Advanced Sensor Research

ADVANCED SENSOR RESEARCH Open Access

www.advsensorres.com

RESEARCH ARTICLE OPEN ACCESS

Hybrid-Printed Single-ChemFET Electronic Nose Enabled by Machine Learning

Hankun Yang[1] | Martin Sommer[2] | Surya Abhishek Singaraju[3] | Pooja Arya[3] | Gabriel Cadilha Marques[3] | Jan Fessler[1] | Jasmin Aghassi-Hagmann[3] | Uli Lemmer[1,2]

[1]Light Technology Institute (LTI), Karlsruhe Institute of Technology (KIT), Karlsruhe, Germany | [2]Institute of Microstructure Technology (IMT), Karlsruhe Institute of Technology (KIT), Eggenstein-Leopoldshafen, Germany | [3]Institute of Nanotechnology (INT), Karlsruhe Institute of Technology (KIT), Eggenstein-Leopoldshafen, Germany

Correspondence: Uli Lemmer (uli.lemmer@kit.edu)

Received: 12 February 2026 | **Revised:** 18 July 2026 | **Accepted:** 27 July 2026

Keywords: aerosoljet printing | ChemFET | electronic nose | gas sensing | inkjet printing | machine learning

ABSTRACT

We present an electronic nose sensor based on a single chemically sensitive field-effect transistor (ChemFET). A novel hybrid printing process that combines the advantages of inkjet and aerosol jet printing is used to fabricate the ChemFET with a semiconducting sub-10 nm In_2O_3 thin-film channel. The sensor was first electrically characterized, showing an on/off ratio of $2.3 \cdot 10^5$ and a threshold voltage of 12.67 V. Three gases at 100 ppm concentration—isopropyl alcohol, benzene, and carbon monoxide–are used to test the sensing capability. We show that a single ChemFET generates gas-specific features across different drain-source (V_{DS}) and gate-source voltages (V_{GS}). Two classification algorithms, linear discriminant analysis (LDA) and random forest (RF), are evaluated using leave-one-out cross-validation. Both algorithms can classify reference air and carbon monoxide without errors, but RF classifies isopropyl alcohol and benzene with higher precision and recall. The feature importance analysis reveals a correlation with V_{GS} and not with V_{DS}. After feature importance-based feature selection, LDA and RF achieve F1-scores of 0.85 and 0.94, respectively. Our findings indicate that the printed single ChemFET-based sensor is a promising candidate for gas-sensing applications.

1 | Introduction

In recent years, demand for cost-effective, reliable gas detection systems has risen significantly amid growing concerns about air quality, industrial safety, and public health [1–3]. In response to these challenges and in contrast to traditional gas-specific sensors, electronic nose (e-nose) technology emerges as a potential solution for detecting a broad spectrum of gases, gas compositions, and odors. Its application areas span from early fire detection and process surveillance to air and food quality monitoring and medical diagnosis [1–4]. The e-nose offers a powerful approach to gas sensing by mimicking the pattern-recognition capabilities of the mammalian olfactory system [4]. An e-nose generally consists of an array of subsensors that respond to a wide range of gaseous molecules such as volatile organic compounds (VOCs). Systematic or randomized differences in the subsensors allow the e-nose to capture gas- and concentration-specific signal patterns. Subsequently, machine learning algorithms are used to distinguish between previously trained gases [4, 5]. Traditional dimensionality reduction techniques such as principal component analysis (PCA) [6–15] and linear discriminant analysis (LDA) [6, 8, 9, 16–18] are efficient and straightforward. They are widely used but struggle with complex non-linear sensor signal patterns and temporal variability [19]. Also, widely used machine learning methods, such as support vector machines (SVMs) [8, 16], and random forests (RFs) [19–23], can handle

more complex data but face challenges when dealing with highly overlapping data [19]. Artificial-neural-network-based methods, including multilayer perceptron (MLP) [23–27], extreme learning machine (ELM) [28, 29], convolutional neural network (CNN) [24, 25, 30, 31], and long short-term memory (LSTM) [32, 33], have been shown to perform well with complex nonlinear data but require extensive training of complex models. This leads to a longer training duration. Additionally, they lack the model transparency and interpretability of the previously mentioned algorithms. The optimal classification algorithm needs to be selected based on the e-nose front-end technology and the specific gas-detection application.

Various sensing mechanisms across different domains exist, including electrical (chemiresistive, capacitive, and field-effect-based), mechanical (surface acoustic wave and quartz crystal microbalance), and optical (colorimetric, fluorescence, and polarization/absorbance) methods [34]. Compared to chemiresistive devices, chemically sensitive field-effect transistor (ChemFET) based sensors stand out for their enhanced sensitivity and selectivity, as well as their lower power consumption [35–39]. Conventional chemiresistive e-noses require multiple subsensors to maximize selectivity and minimize cross-sensitivity. Alternatively, using a few or only one subsensor, the required features can be generated by sweeping the operating temperature [40, 41]. The downside of this approach is the significantly reduced measurement cycle frequency depending on the thermal design and power budget. In contrast, ChemFET-based devices may require fewer, or only a single subsensor, as features are extracted by sweeping the gate-source and drain-source voltages [42]. Furthermore, this method may replace conventional excitation approaches such as heating or UV irradiation, resulting in power savings compared to chemiresistive approaches. Although ChemFETs are also being developed for liquid analytes, they generally perform much better with gaseous samples [43]. Two distinct ChemFET design variants exist. The exposed-gate variant uses a conventional top-gate transistor structure. Commonly, a metal is used as the gate material, such as palladium, whose work function changes when exposed to different analytes. In return, the change in the transistor's characteristics can be measured [43]. The exposed channel variant directly uses the channel semiconductor as the sensing material [43]. This usually results in higher sensitivity than the exposed-gate variant. For ChemFETs, different channel materials can be used, ranging from semiconducting polymers (polyaniline and polystyrenesulfonic acid [44]) to carbon allotropes (graphene [45], single-walled carbon nanotubes [46]) to inorganic metal oxide semiconductors such as SnO_2 nanowires [47, 48]. Among the metal oxides, In_2O_3 is a promising candidate for ChemFET applications because it is a printable n-type semiconductor that has been successfully employed as a thin-film transistor channel material [49–53]. Simultaneously, In_2O_3 is used as an effective gas-sensing material in chemiresistive sensors [54–57].

Printed electronics is a rapidly evolving field that utilizes various additive techniques to fabricate electronic devices. Printing enables cost-effective large-area scaling and improves design flexibility for both layout and substrate choice. Some examples are screen printing, inkjet printing (IJP), aerosol jet printing (AJP), and ultra-precise dispensing (in order of decreasing minimum feature size). In our approach, we combine IJP and AJP. IJP can be used to print functional materials needed for electronics. With optimized IJP, precise layer heights in the nanometer range can be achieved, which is required, for example, for the fabrication of thin-film transistors. Meanwhile, an aerosol jet printer atomizes the ink into a fine mist, which is transported to the substrate by a carrier gas stream. Furthermore, the aerosol jet stream is precisely guided and focused onto the substrate with an enveloping sheath gas stream. The AJP is better suited for printing fine electrodes due to its continuous jetting, compared to the IJP's drop-wise deposition. Additionally, the AJP can print a wider range of inks with viscosities up to 1000 cP (1 cP = 10^{-3} Pa s) while being significantly less susceptible to nozzle clogging because of the protective sheath gas stream [58]. Combining the advantages of both printing technologies can satisfy the demand for rapid development of functional multi-material devices, such as the e-nose.

Hence, in our work, we develop an e-nose that uses a single ChemFET sensor fabricated via a novel hybrid inkjet-aerosol jet approach. The sensor data is evaluated with two different machine learning algorithms. We show that a random forest approach leads to the best classification results.

2 | Results and Discussion

2.1 | Printing and FET Characteristics

The ChemFETs are structured as bottom-gate thin film transistors (TFTs). The layer stack and its fabrication route, as well as a schematic cross-section, are illustrated in Figure 1a,b. In this work, the semiconducting channel material, In_2O_3, is fabricated via a precursor route. IJP is chosen as a precise deposition method. The film thickness can be further fine-tuned by adjusting the precursor concentration and the DPI setting. Using a stylus profilometer, the In_2O_3 film thickness was determined to be below 10 nm after annealing at 300°C. The ChemFETs were intentionally fabricated without top passivation to allow gas interactions with the semiconductor thin film. Top electrodes consisting of Ag nanoparticles (Ag-NPs) were printed using AJP with micrometer-thicknesses for higher conductivity. Direct contact between Ag and In_2O_3 has been reported to form a disadvantageous Schottky barrier [59]. In contrast, Ag on indium tin oxide (ITO) contacts have been successfully employed with no reports of Schottky behavior [60, 61]. Hence, an intermediate ITO layer was aerosol jet printed. The details of the fabrication steps are described in Section 4 and are illustrated in Figure 1a. A microscope image of the fabricated chip is shown in Figure 1c. The channel length and width are 50 and 550 µm, respectively. A focused ion-beam cross-sectional SEM image is shown in Figure S1. This hybrid additive fabrication method, using two different digital printing modalities, efficiently overcomes the challenge of vastly different layer thickness requirements across layers.

The electrical characterization of a ChemFET via output and transfer characteristics measurements under reference air conditions is shown in Figure 2. In the output characteristic (Figure 2a), both the linear and saturated regions are visible. The maximum measured current was 71.62 µA at V_{DS} = 30 V and V_{GS} = 30 V. From the transfer characteristic at V_{DS} = 30 V (Figure 2b), an on/off ratio of $2.3 \cdot 10^5$ is extracted. With the linear extrapolation

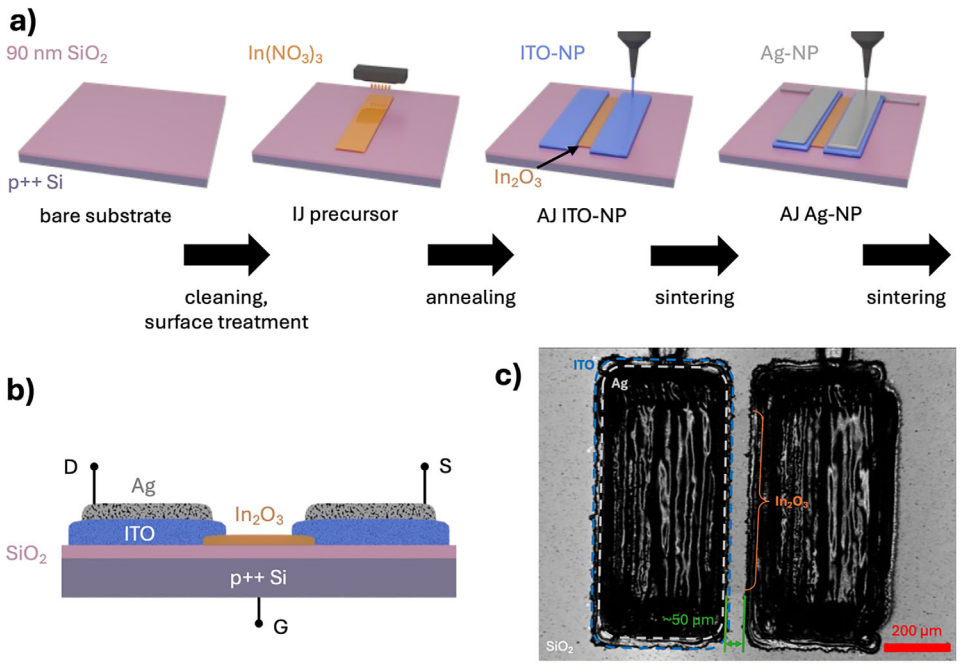

FIGURE 1 | Layer structure of ChemFET and fabrication process. (a) Fabrication process including inkjet printing of the In_2O_3 precursor for the channel semiconductor and aerosol jet printing of ITO and Ag nanoparticles as electrodes. (b) Cross-section layout of a single ChemFET with source (S), drain (D), and gate (G) contacts. (c) Light microscope image of a single ChemFET. The In_2O_3 thin film is slightly darker than the SiO_2 background.

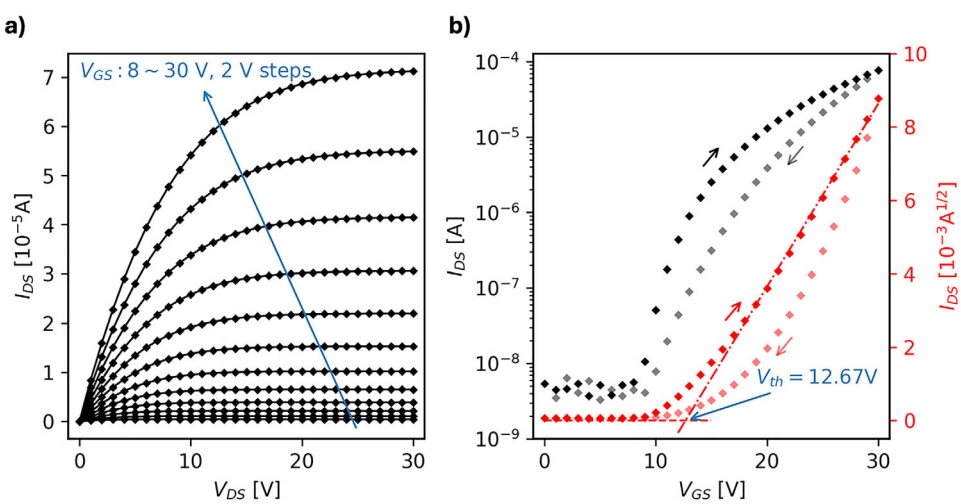

FIGURE 2 | Characteristics of the printed ChemFET. (a) output characteristics with $\Delta\ V_{GS} = 2\ V$ steps, (b) transfer characteristics at $V_{DS} = 30$ V. The ChemFET is measured at room temperature using reference air (50% RH, 500 sccm).

method, the threshold voltage $V_{th} = 12.67$ V is calculated for the forward sweep.

Non-negligible hysteresis effects are observed in the transfer characteristics. However, this is not necessarily a detrimental characteristic for e-nose applications. On the contrary, the hysteresis may yield additional information that can be advantageous for the classification. The observed threshold-voltage drift over prolonged measurements is more critical. For TFTs, this transient change in threshold voltage $\Delta V_{th}(t)$ is caused by charge trapping and can be modeled by a stretched-exponential function (refer to Equation S1) [62]. The threshold voltage change over 14 h is shown in Figure S2. Initially, the threshold voltage shifts rapidly but stabilizes around 2 h after the start of the measurement. Relevant gas measurements are performed after a stabilization time of at least 8 h.

2.2 | Gas Sensing Measurements

To evaluate the ChemFET's gas-sensing capability, its characteristics are continuously recorded as it is sequentially exposed to reference air, isopropyl alcohol, benzene, and carbon monoxide. The relative humidity and the gas concentration are kept constant

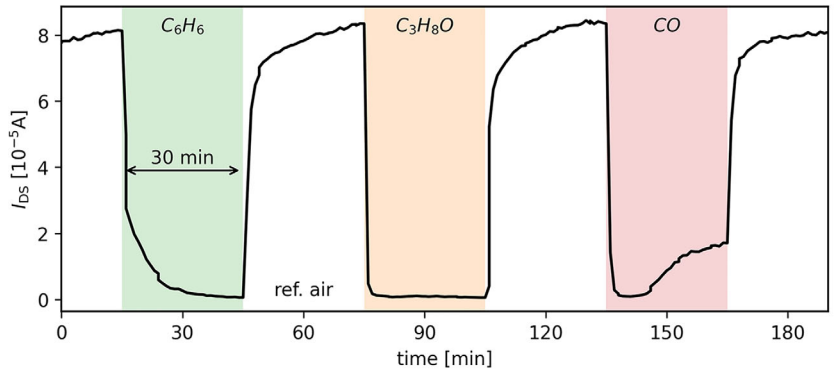

FIGURE 3 | Representative transient response of the ChemFET. The three gases, benzene (C_6H_6), isopropyl alcohol (C_3H_8O), and carbon monoxide (CO), are measured in addition to the baseline measurements of reference air. The ChemFET is operated at V_{DS} = 30 V and V_{GS} = 30 V.

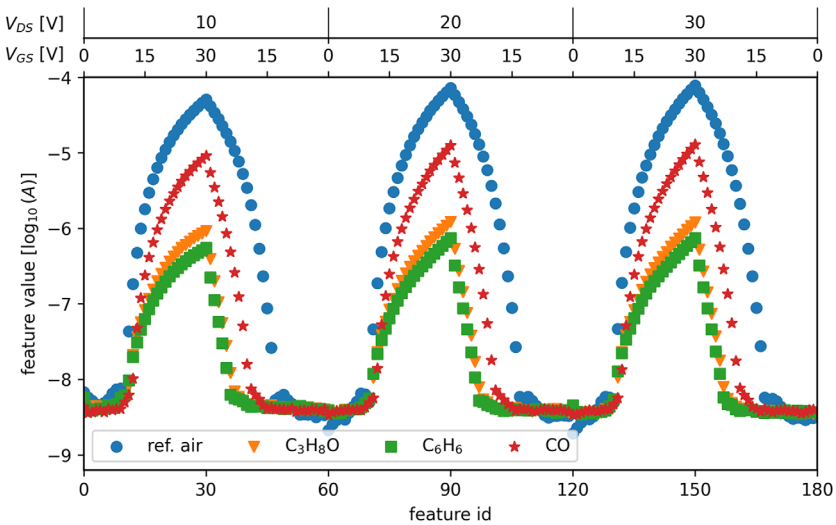

FIGURE 4 | Feature pattern comparison between all four different classes. The corresponding V_{DS} and V_{GS} values for each feature are displayed at the top of the plot.

at 50% and 100 ppm, respectively. Each measurement segment lasts 30 min. A representative transient response of the ChemFET sensor at the operating point V_{DS} = 30 V and V_{GS} = 30 V is shown in Figure 3. Relative to the reference air baseline, the I_{DS} values of all measured gases decrease rapidly after exposure. The stabilized end values of benzene (green) and isopropyl alcohol (orange) are similar, whereas carbon monoxide has a higher end value.

Different concentrations have been measured in a separate measurement series, and the combined results are presented in Figure S4. The transient I_{DS} response of the ChemFET depends not only on the analyte but also on the concentration, as shown in Figure S4a.

A limited growth model according to Equation S2 was fitted to extract the signal response, and the response and recovery times for each concentration and segment as detailed in Section 4. The ChemFET responds within approx. 4 to 8 min on average, depending on the analyte, as shown in Figure S4b. Recovery takes consistently longer, ranging between 6 and 9 min on average. The ChemFET's sensitivities toward IPA and benzene are quite similar, and nearly two orders of magnitude higher than that toward CO, as shown in Figure S4c. Benzene exhibits the lowest LoD value of 1 to 2 ppm, whereas the LoD for CO averages between 4 and 5 ppm, as shown in Figure S4d. Additionally, all extracted metrics exhibit significant standard deviations, which may be attributed to noise and drift, as shown in Figure S5.

2.3 | Classification and Model Evaluation

A single data point consists of three sequentially measured transfer characteristics at V_{DS} = 10, 20, and 30 V. V_{GS} is swept from 0 to 30 V and back in 1 V increments during each transfer measurement. Consequently, each measurement cycle includes 180 I_{DS} values. These I_{DS} values of the different classes are compared in Figure 4. The presented feature patterns are averaged from all samples of each class. In the range of 0V ≤ V_{GS} ≤ 10 V (i.e. V_{GS}<V_{th}), no significant differences are observed between the classes. In contrast, notable variations occur when increasing V_{GS} beyond 10 V. Reference air and carbon monoxide are clearly distinguished from isopropyl alcohol and benzene. Interestingly, they differ not only in maximum value but also in the symmetry of the curves, which in turn indicates differences

in hysteresis for the respective gas. Isopropyl alcohol and benzene show very similar patterns, with only minor differences.

The complete extracted dataset consists of the feature matrix $X \in \mathbb{R}^{n \times m}$ and the matching label array $y \in G^n$. Here, n is the number of data samples, $m = 180$ the number of features, and $G \in$ {reference air, isopropyl alcohol, benzene, CO} the set of labels. A total of $n = 820$ samples are taken. The reference air class accounts for approximately 59% of the data, while the remaining 41% is distributed almost equally between isopropyl alcohol, benzene, and carbon monoxide. This imbalance is due to the more frequent occurrence of reference air segments. For each measurement cycle, all 180 recorded I_{DS} values are logarithmically transformed (base 10) and stored as a single sample. The reason behind the logarithmic transformation is to nonlinearly improve the feature distinction between the gas classes. Preliminary tests showed increased classification performance of logarithmically transformed datasets. Relevant datasets at the stabilized regions of each measured gas segment are extracted and labeled accordingly.

In this work, LDA and RF are selected for training and testing on the extracted dataset. LDA is a statistical, supervised machine learning method, first introduced by Fisher in 1936 [63] and remains one of the most widely used algorithms for e-nose applications [4, 5]. In our past work, we also successfully used LDA specifically for e-nose applications [64, 65]. Meanwhile, previous reports indicate that RF is another top-performing classification algorithm for e-nose applications [19–21, 23]. Compared to LDA, which assumes normal data distribution, RF may perform better on non-normally distributed data.

LDA finds the optimal projection matrix W, which linearly transforms the data from the feature space $\mathbb{R}^m$ to a lower-dimensional discriminant space. In this discriminant space, the ratio of between-class to within-class variance is maximized. This maximization task can be reduced to an eigenvalue/eigenvector problem as stated in Equation (1) [66, 67].

$$\arg\max_{W} \frac{W^T S_b W}{W^T S_w W} \Rightarrow S_w W = \lambda S_b W \tag{1}$$

Here, S_b and S_w are the between- and within-class scatter matrices, respectively. An alternative approach replaces S_w with the total covariance matrix.

RF is a supervised machine learning method that consists of multiple decision trees (DTs), which contain nodes arranged in a tree-like structure. The decision path starts at the initial root node, traverses through branch nodes, and ultimately ends at leaf nodes that predict the class. A predefined metric, such as Gini impurity (GI), determines the order and branching of features at each node. A feature with high GI indicates low informational gain. Therefore, the DT is constructed by minimizing the GI. While a single decision tree can independently classify data, the RF mitigates the DT-typical problems of high variability and overfitting by using the bagging (bootstrap aggregating) method. Each DT of an RF is trained using a bootstrapped (uniform sampling with replacement) subset of the whole training set. The final prediction is obtained by aggregating the predictions of all DTs.

The data flow for the model evaluation is described in the following section and depicted in Figure 5. First, the dataset is being balanced by randomized undersampling. Consequently, each class in the balanced dataset contains the same number (111) of samples. Due to the relatively small sample size, the leave-one-out cross-validation (LOOCV) method is chosen to train and evaluate the models. In each LOOCV iteration, the RF is hyperparameter-tuned and trained while the LDA is only trained. Both models are subsequently tested with the single left-out sample. Finally, classification metrics are evaluated for both models.

2.3.1 | Linear Discriminant Analysis vs. Random Forest

To visualize the different classes in the discriminant space, the LDA plot of a representative LDA model, which has been trained on the complete dataset, is shown in Figure 6a. In the LDA plot, the data clusters of reference air (blue) and carbon monoxide (red) are well separated from those of other classes. Likewise, the trained LDA models in the LOOCV achieve, without exception, 1.0 precision and recall for both classes, as shown in the confusion matrix (Figure 7a) and classification report (Table S1). In contrast, the data clusters of isopropyl alcohol and benzene overlap severely in the first two discriminants. Only the third discriminant can separate the two classes to some extent, as shown in Figure 6b. Therefore, the confusion matrix (Figure 7a) shows a high number of misclassifications between these two classes, resulting in relatively low precision and recall values of 0.63–0.67 (see Table S1). All in all, the LDA achieves a macro-averaged F1-score of 0.82.

Compared to LDA, an RF includes hyperparameters that are tuned in a first step in each iteration. Here, the number of trees, the maximum tree depth, the minimum samples required for a split at a node, the minimum samples required for a leaf node, and the maximum number of leaf nodes are included in the hyperparameter tuning. The exact range of each hyperparameter is listed in Table S2. Both reference air and carbon monoxide are again perfectly classified as shown in the confusion matrix in Figure 7b, resulting in precision and recall scores of 1.0 for both classes (refer to Table S1). Approximately 24% of the tested isopropyl alcohol is being misclassified as benzene, whereas only 8% of benzene is misclassified as isopropyl alcohol. On average, the RF algorithm achieves an F1-score of 92%, as shown in Table S1.

Both LDA and RF can accurately classify reference air and CO, indicating that these classes exhibit unique feature patterns that are already visible in the raw features (see Figure 4). Conversely, LDA struggles to classify both benzene and isopropyl alcohol reliably. In comparison, RF increases the class-specific F1-scores by 0.17 and 0.21 for isopropyl alcohol and benzene, respectively. The reduction of misclassification of benzene is most notable. According to these metrics, RF is the better algorithm for the tested ChemFET in combination with the tested gases. But this advantage comes at the cost of extended training duration,

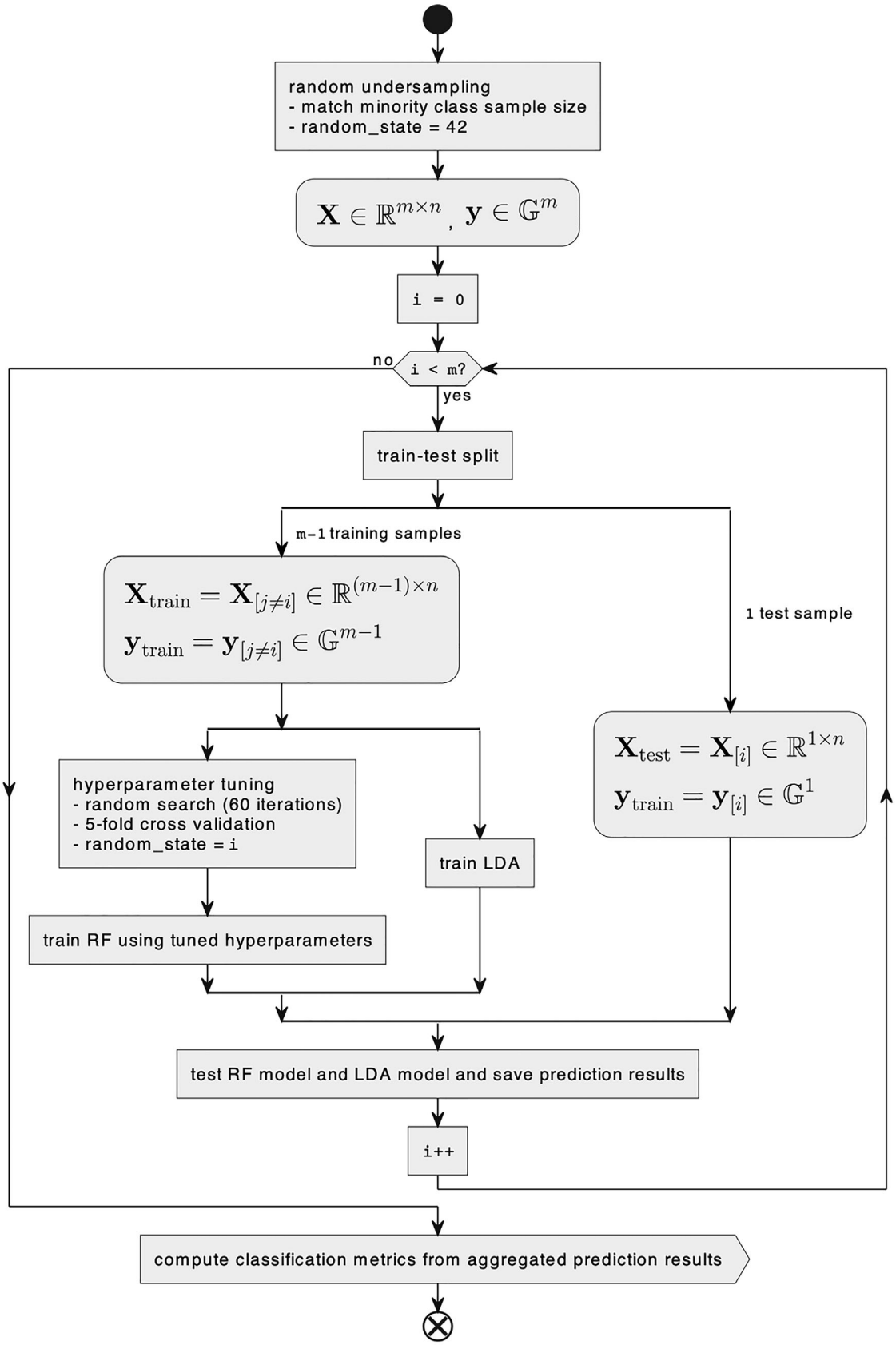

FIGURE 5 | Flow chart of the evaluation. Here, $\mathbb{G}^m$ is the set of classes. During each iteration of the LOOCV loop, the random_state variable is set to the current loop index i for reproducibility.

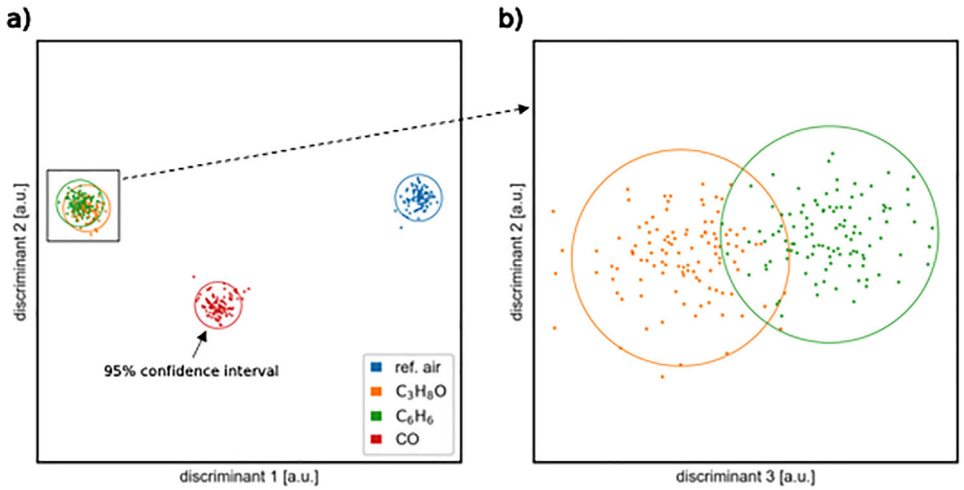

FIGURE 6 | LDA maps of an LDA model that is trained on all samples. (a) LDA map of the first (x) and second-ranked (y) discriminants, including all gas classes. (b) LDA map of the second (y) and third-ranked (x) discriminants that focuses only on Isopropyl alcohol and benzene. The discriminant axes are scaled such that 95% confidence intervals are represented as circles around the class centers.

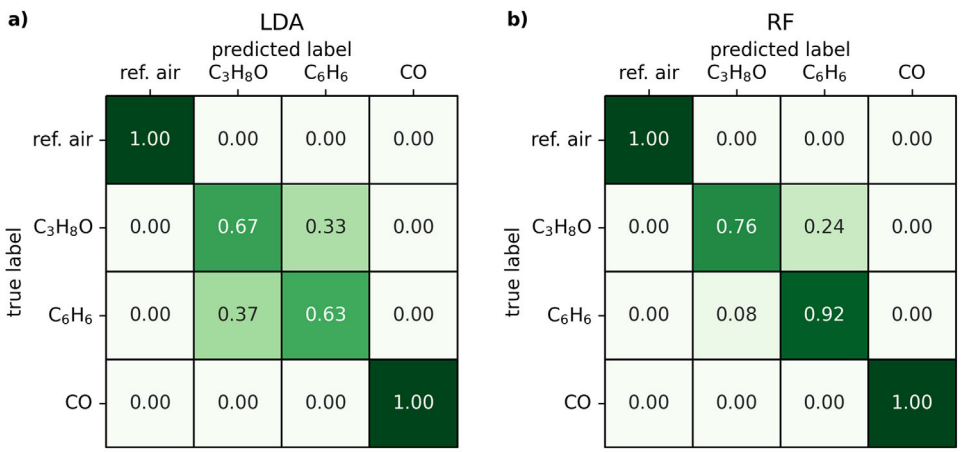

FIGURE 7 | Normalized confusion matrices of LDA (a) and RF (b) after LOOCV.

especially during the hyperparameter optimization step, which the LDA does not require.

2.4 | Sensing Mechanism and Feature Importance Analysis

The proposed sensing mechanism of the presented ChemFET is a combination of:

1. Chemiresistive-Like adsorption and desorption interactions between the analyte molecules and the exposed semiconductor (In_2O_3) channel and
2. The gate-voltage-modulated change in adsorption and desorption dynamics.

To investigate these mechanisms at different operating points, a theoretical band diagram is drawn in Figure 8 and a feature importance analysis is conducted (see Figure 9 and Figure S6).

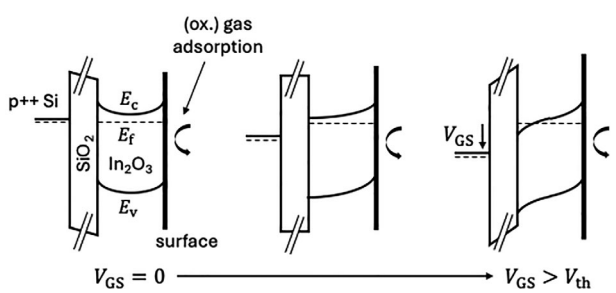

FIGURE 8 | Band diagram of the ChemFET at different operating points. The gate voltage is increased from left to right. A thin In_2O_3 layer enables mutual influence between gas adsorption and gate-voltage modulation. An oxidizing gas is used as an example.

Because of the LOOCV, permutation feature importance cannot be used. Instead, for LDA, the feature importances are computed as the normalized contributions of each feature in the projection matrix W. For RF, the impurity-based feature importances are

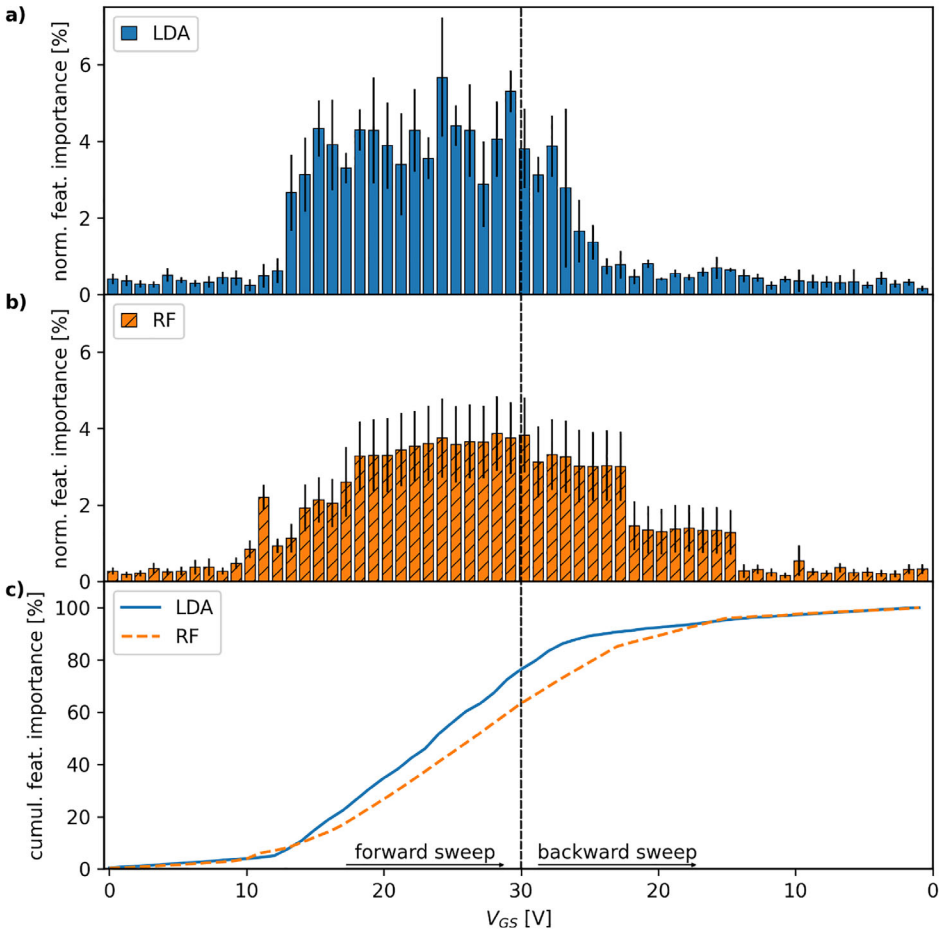

FIGURE 9 | Gate-voltage-dependent feature importance analysis. (a, b) Normalized feature importances of LDA and RF, respectively. c) Cumulative feature importances.

already calculated and stored during training. Figure 9 and Figure S6 correlate feature importance with V_{GS} and V_{DS}, respectively.

2.4.1 | Off-State

In the off-state, the ChemFET can be regarded as a chemiresistor. A measurable change in conductivity occurs due to the change in charge-carrier density, as shown on the left side of Figure 8. Therefore, the same sensing and selectivity mechanisms apply as for chemiresistors, including adsorption and desorption interactions (oxidizing and reducing gases) and the displacement of other reactive species [68, 69]. Our feature importance analysis shows that, for both LDA (a) and RF (b), the feature importances are near zero for $V_{GS} < V_{th}$. This is attributed to the lack of external excitation, such as heating or UV irradiation, combined with very low current values. Therefore, under these operating conditions, a practical use of the ChemFET as a chemiresistor in its off-state is not possible.

2.4.2 | On-State

This limitation is circumvented by creating a conducting channel inside the semiconductor by elevating the V_{GS} above V_{th}. Here, the positive gate voltage accumulates electrons near the semiconductor-insulator interface, thereby forming a conductive channel. If the semiconductor thickness is sufficiently small, the change in gas adsorption-induced charge-carrier density extends far enough into the voltage-modulated channel, as indicated by the band bending in Figure 8. As a result, the transistor characteristics change, and the variation of I_{DS} can be measured as the sensor signal. This gas-induced change in transistor characteristics, also known as ambient stress, is usually undesirable and reduces the FET's reliability [62]. But for the ChemFET application in this work, it is specifically exploited to enable gas sensing. Because of the exposed semiconducting and chemiresistive thin-film structure, the ChemFET's selectivity for different gases in the on-state is partially explained by the previously mentioned mechanisms for the chemiresistor. But more importantly, the gate bias introduces electroadsorptive effects, which impact the adsorption and desorption dynamics of different gases. This can, e.g., be explained by the reduction and oxidation of gas molecules, which in turn enable or enhance certain catalytic reactions and shift the density equilibrium of surface-adsorbed gas molecules [70, 71].

In the feature importance analysis (Figure 9), the feature importance rises with V_{GS} in the range $V_{GS} > V_{th}$. This observed increase in feature importance, and consequently the ChemFET's selectivity at higher gate voltages (Figure 9), is consistent with

the reported electroadsorptive mechanisms. Furthermore, the observed feature importances during the backward sweep, despite being asymmetric, indicate hysteresis's informational gain and discriminative power. This observation is also consistent with previous reports, but no definitive explanation for this effect has been identified yet [72]. Further studies are needed to unravel the underlying mechanisms.

In contrast to V_{GS}, no significant dependence was observed between the feature importance and V_{DS} (refer to Figure S6).

2.4.3 | Feature Selection

The results from the feature importance analysis can be used in practice to drive improvements. For example, future measurements may omit operation regimes with low informational gain, such as the off-state. Here, we instead virtually filter out a certain lower percentile of the initial 180 features. To find the optimal threshold, filtering is performed for multiple percentile values, sweeping from 0.05 to 0.50 in 0.05 steps. During this, the RF is not hyperparameter-tuned again but uses the averaged hyperparameters as listed in Table S2. Within the quantile range and resolution, both LDA and RF achieve the maximum F1-scores at $p = 0.35$. Minor improvements are observed for both models. The F1-score of LDA and RF increases from 0.83 to 0.85 and from 0.92 to 0.94, respectively. This finding indicates that approximately a third of the features do not provide informational gain. At the same time, the noise from these features is not overly disruptive, which would lead to a higher F1-score gain after feature selection. The findings from the feature analysis indicate that a subset of operation points (combination of V_{DS} and V_{GS}) is sufficient to yield similar results, while having the advantage of faster measurement cycles.

3 | Conclusion

In this study, an electronic nose sensor based on a single ChemFET was successfully fabricated using a hybrid digital printing approach. A nanometer-thick, semiconducting In_2O_3 film serving as a channel, exposed to different gases, was inkjet-printed, while the source and drain electrodes were aerosol-jet-printed. The FET characteristics, on/off-ratio and threshold voltage, were measured to be $2.3 \cdot 10^5$ and 12.67 V, respectively. The e-nose was operated at room temperature with no external excitation such as heating or UV irradiation. To test the e-nose, three different gases—isopropyl alcohol, benzene, and carbon monoxide—were measured alongside reference air. The gate-source is swept for three drain-source voltages to generate 180 features per sample. Using this data, two classification algorithms, LDA and RF, were trained, tested, and compared. Both algorithms correctly classify reference air and carbon monoxide with no errors. LDA, however, misclassifies isopropyl alcohol and benzene, resulting in mediocre overall classification performance with an F1-score of 0.85. Meanwhile, RF shows improved precision and recall for isopropyl alcohol and especially for benzene. This results in an overall increase in the F1-score to 0.94 for RF. This is enabled by feature selection based on feature importances, which is shown to correlate with V_{GS} for $V_{GS} > 10$ V.

4 | Experimental Section

4.1 | Fabrication—Ink Preparation

An indium nitrate hydrate-based precursor ink was used to fabricate the In_2O_3 thin film, based on previous reports by Singaraju [73–75]. The solvent was composed of one part glycerol and four parts deionized water, by weight. 0.05 M indium nitrate hydrate ($In(NO_3)_3$) (≥ 99.99%, Thermo Scientific) was then added to the solvent and magnetically stirred overnight to obtain a transparent ink. The concentration was optimized to enable stable printability and to achieve the desired film thickness. Using a rotational viscosimeter (Anton Paar ViscoQC300L), the viscosity of the precursor ink was determined to be 2.1 cP. The nanoparticle-based ITO ink (ITO nanoparticle water dispersion, 18 nm, 20 wt.%, In:Sn = 90:10 in wt.%, US Research Nanomaterials) and the nanoparticle-based Ag ink (JS-A221AE, Novacentrix) were used as purchased with no further modifications.

4.2 | Fabrication–Deposition

First, a p-doped Si wafer comprising a 90 nm SiO_2 layer was diced and subsequently cleaned in an ultrasonic bath for 10 min each in acetone and isopropyl alcohol. The cleaned substrates were then plasma-activated to adjust the surface wetting behavior for the subsequent IJP process.

The In_2O_3 precursor was printed onto the cleaned and surface-treated substrates using a research-class inkjet printer (SUSS LP50 PiXDRO) with a 1 pL droplet volume cartridge (DMC-11601). During printing, the nozzle and plate temperatures were set to 30°C and 40°C, respectively. The ejection frequency was kept at 3 kHz. The thin film was printed with 800 DPI. After printing, the layer was dried at 150°C for 5 min and annealed at 300°C for 1 h on a hotplate in ambient air.

The ITO-NP and Ag-NP inks were both printed with an aerosol jet printer (AJ 5X, Optomec). The sheath-to-ink flow ratios for ITO and Ag inks were set to 6.5:1 and 4:1, respectively. The printing speed was kept at 5 mm/s for all prints. Printed ITO structures were first dried at 80°C for 10 min and subsequently sintered at 300°C for 1 h. Printed Ag structures were sintered directly at 200°C for 1 h without a preceding drying step to prevent cracks from forming. All drying and sintering steps were performed on hot plates under ambient conditions. The printed structures are measured using a stylus profilometer (DektakXT, Bruker) with a 0.2 µm lateral resolution.

4.3 | Measurement

Both the gate-source voltage (V_{GS}) and the drain-source voltage (V_{DS}) were controlled by a power supply (Rigol DP832A) with the common ground connected to the source. The transfer measurement was performed via a forward and a backward V_{GS} sweep in 1 V increments. A total measurement cycle consisted of three transfer characteristics measurements at V_{DS} = 10, 20, and 30 V. The drain-source current (I_{DS}) was measured by a multimeter (Keithley 2001) and logged on a measurement PC using PyVISA (Python) at each combination of V_{DS} and V_{GS}.

Figure S3 depicts the experimental setup. Dry reference air was supplied by a "zero-air-generator" (TG 12-UP, Sylatech). The reference air was humidified using a bubbler in a controlled manner. Three mass-flow controllers (MFCs) control the gas flows. MFC_1 for the humidified air, MFC_2 for the dry air, and MFC_3 for the gases supplied by the gas bottles. For a target flow Q_{target}, gas concentration $c_{gas,\,target}$, and relative humidity RH_{target}, the three flow rates Q_1, Q_2, and Q_3 were adjusted accordingly. The gas was then directed to the e-nose, which is installed in a custom-designed housing with pogo-pins contacting the top electrodes of the ChemFET. The sensor was operated at room temperature without any external excitation such as heating or UV irradiation. Finally, the gases were disposed of in a fume hood. Reference air at 50% RH was measured as the baseline. Three gases, including isopropyl alcohol, carbon monoxide, and benzene, each at 50% RH and 100 ppm were individually measured in a randomized order with the same occurrence frequency. Each measurement segment was 30 min long. Baseline (reference air, 50%RH, 30 min) measurements were conducted between the gas measurement segments. The flow rate was fixed at 500 sccm.

4.4 | Data Analysis

Data analysis was performed using Python (3.12). For all mentioned functions, default parameters were used if not otherwise stated. The initial I_{DS} was logarithmically transformed. Randomized undersampling was performed using RandomUnderSampler from imblearn (0.14.0), with random_state set to 42 for repeatability. Subsequently, LOOCV was performed using the scikit-learn (1.7.2) class LeaveOneOut. The LDA algorithm was implemented according to Henrion and Henrion [76]. RandomForestClassifier (scikit-learn) was used as the RF algorithm. The RF was hyperparameter-tuned using RandomizedSearchCV (scikit-learn) with 60 iterations and 5-fold stratified cross-validation. The random_state of RandomizedSearchCV was set to the current LOOCV loop index. After testing, the confusion matrix and classification metrics were computed from the accumulated results of LOOCV using the functions confusion_matrix and classification_report (scikit-learn).

4.5 | Sensing Properties

The 90% response and recovery times are calculated according to Equation S3. Because of the decreasing nature of the responses, the absolute response values are converted into dimensionless relative responses according to Equation S4. The gas-dependent sensitivities are then calculated by computing the slope of the linear regression of the concentration-dependent relative response values. Finally, the limit of detection is extracted for each analyte by intersecting the local linear interpolation and the noise level.

Acknowledgments

The authors gratefully acknowledge the Deutsche Forschungsgemeinschaft (DFG, German Research Foundation) under Germany's Strategy via the Excellence Cluster 3D Matter Made to Order (3DMM2O, EXC-2082/1–390761711; EXC-2082/2–390761711) and the Carl Zeiss Foundation for financial support.

Open access funding enabled and organized by Projekt DEAL.

Funding

This work was funded by the Deutsche Forschungsgemeinschaft (3DMM2O, EXC-2082/1-390761771; EXC-2082/2-390761711).

Conflicts of Interest

The authors declare no conflicts of interest.

Data Availability Statement

The data that support the findings of this study are available from the corresponding author upon reasonable request.

References

1. S. Panda, S. Mehlawat, N. Dhariwal, A. Kumar, and A. Sanger, "Comprehensive Review on Gas Sensors: Unveiling Recent Developments and Addressing Challenges," *Materials Science and Engineering: B* 308 (2024): 117616, https://doi.org/10.1016/j.mseb.2024.117616.

2. H. T. Jung, "The Present and Future of Gas Sensors," *ACS Sensors* 7 (2022): 912–913, https://doi.org/10.1021/acssensors.2c00688.

3. S. Dhall, B. R. Mehta, A. K. Tyagi, and K. Sood, "A Review on Environmental Gas Sensors: Materials and Technologies," *Sensors International* 2 (2021): 100116, https://doi.org/10.1016/j.sintl.2021.100116.

4. C.-D. Kohl and T. Wagner, eds., *Gas Sensing Fundamentals* (Springer, 2014), https://doi.org/10.1007/978-3-642-54519-1.

5. T. Liu, L. Guo, M. Wang, et al., "Review on Algorithm Design in Electronic Noses: Challenges, Status, and Trends," *Intelligent Computing* 2 (2023): 0012, https://doi.org/10.34133/icomputing.0012.

6. G. G. Teixeira, L. G. Dias, N. Rodrigues, et al., "Application of a Lab-Made Electronic Nose for Extra virgin Olive Oils Commercial Classification According to the Perceived Fruitiness Intensity," *Talanta* 226 (2021): 122122, https://doi.org/10.1016/j.talanta.2021.122122.

7. Z. Mao, J. Wang, Y. Gong, H. Yang, and S. Zhang, "A Set of Platforms with Combinatorial and High-Throughput Technique for Gas Sensing, From Material to Device and to System," *Micromachines* 9 (2018): 606, https://doi.org/10.3390/mi9110606.

8. A. Jiarpinijnun, K. Osako, and U. Siripatrawan, "Visualization of Volatomic Profiles for Early Detection of Fungal Infection on Storage Jasmine Brown Rice Using Electronic Nose Coupled with Chemometrics," *Measurement* 157 (2020): 107561, https://doi.org/10.1016/j.measurement.2020.107561.

9. Q. Chen, Z. Chen, D. Liu, Z. He, and J. Wu, "Constructing an E-Nose Using Metal-Ion-Induced Assembly of Graphene Oxide for Diagnosis of Lung Cancer via Exhaled Breath," *ACS Applied Materials & Interfaces* 12 (2020): 17713–17724, https://doi.org/10.1021/acsami.0c00720.

10. V. S. Palaparthy, S. N. Doddapujar, S. G. Surya, et al., "Hybrid Pattern Recognition for Rapid Explosive Sensing with Comprehensive Analysis," *IEEE Sensors Journal* 21 (2021): 8011–8019, https://doi.org/10.1109/JSEN.2020.3047271.

11. C. Zhou, Z. Wu, Y. Guo, et al., "Ultrasensitive, Real-Time and Discriminative Detection of Improvised Explosives by Chemiresistive Thin-Film Sensory Array of Mn^{2+} Tailored Hierarchical ZnS," *Scientific Reports* 6 (2016): 25588, https://doi.org/10.1038/srep25588.

12. Q. Liu, N. Zhao, D. Zhou, et al., "Discrimination and Growth Tracking of Fungi Contamination in Peaches Using Electronic Nose," *Food Chemistry* 262 (2018): 226–234, https://doi.org/10.1016/j.foodchem.2018.04.100.

13. A. Shanmugasundaram, S. V. Manorama, D. S. Kim, Y. J. Jeong, and D. Weon Lee, "Toward Point-Of-Care Chronic Disease Management: Biomarker Detection in Exhaled Breath Using an E-Nose Sensor Based on rGO/SnO_2 Superstructures," *Chemical Engineering Journal* 448 (2022): 137736, https://doi.org/10.1016/j.cej.2022.137736.

14. S. J. Kim, S. J. Choi, J. S. Jang, H. J. Cho, and I. D. Kim, "Innovative Nanosensor for Disease Diagnosis," *Accounts of Chemical Research* 50 (2017): 1587–1596, https://doi.org/10.1021/acs.accounts.7b00047.

15. X. Pan, J. Chen, X. Wen, et al., "A Comprehensive Gas Recognition Algorithm with Label-Free Drift Compensation Based on Domain Adversarial Network," *Sensors and Actuators B: Chemical* 387 (2023): 133709, https://doi.org/10.1016/j.snb.2023.133709.

16. T. Julian, S. N. Hidayat, A. Rianjanu, A. B. Dharmawan, H. S. Wasisto, and K. Triyana, "Intelligent Mobile Electronic Nose System Comprising a Hybrid Polymer-Functionalized Quartz Crystal Microbalance Sensor Array," *ACS Omega* 5 (2020): 29492–29503, https://doi.org/10.1021/acsomega.0c04433.

17. E. K. Tang, P. N. Suganthan, X. Yao, and A. K. Qin, "Linear Dimensionality Reduction Using Relevance Weighted LDA," *Pattern Recognition* 38 (2005): 485–493, https://doi.org/10.1016/j.patcog.2004.09.005.

18. Q. Zhang, S. Zhang, C. Xie, et al., "Characterization of Chinese Vinegars by Electronic Nose," *Sensors and Actuators B: Chemical* 119 (2006): 538–546, https://doi.org/10.1016/j.snb.2006.01.007.

19. Y. Tan, Y. Chen, Y. Zhao, et al., "Recent Advances in Signal Processing Algorithms for Electronic Noses," *Talanta* 283 (2025): 127140, https://doi.org/10.1016/j.talanta.2024.127140.

20. N. S. S. Capman, X. V. Zhen, J. T. Nelson, et al., "Machine Learning-Based Rapid Detection of Volatile Organic Compounds in a Graphene Electronic Nose," *ACS Nano* 16 (2022): 19567–19583, https://doi.org/10.1021/acsnano.2c10240.

21. V. Schroeder, E. D. Evans, Y.-C. M. Wu, et al., "Chemiresistive Sensor Array and Machine Learning Classification of Food," *ACS Sensors* 4 (2019): 2101–2108, https://doi.org/10.1021/acssensors.9b00825.

22. P. Shakya, E. Kennedy, C. Rose, and J. K. Rosenstein, "High-Dimensional Time Series Feature Extraction for Low-Cost Machine Olfaction," *IEEE Sensors Journal* 21 (2020): 2495–2504, https://doi.org/10.1109/JSEN.2020.3022966.

23. S. Qiu, J. Wang, C. Tang, and D. Du, "Comparison of ELM, RF, and SVM on E-Nose and E-Tongue to Trace the Quality Status of Mandarin (Citrus unshiu Marc.)," *Journal of Food Engineering* 166 (2015): 193–203, https://doi.org/10.1016/j.jfoodeng.2015.06.007.

24. P. Peng, X. Zhao, X. Pan, and W. Ye, "Gas Classification Using Deep Convolutional Neural Networks," *Sensors* 18 (2018): 157, https://doi.org/10.3390/s18010157.

25. S. Braun, A. Kobald, A. Oprea, et al., "Monitoring Hand Hygiene with Commercial Gas Sensors: A Pattern Recognition Approach," *Sensors and Actuators B: Chemical* 352 (2022): 131027, https://doi.org/10.1016/j.snb.2021.131027.

26. Y. Yang and L. Wei, "Application of E-Nose Technology Combined with Artificial Neural Network to Predict Total Bacterial Count in Milk," *Journal of Dairy Science* 104 (2021): 10558–10565, https://doi.org/10.3168/jds.2020-19987.

27. M. Li, H. Liu, J. Chang, et al., "Quantitatively Discriminating Alcohol Molecules by Thermally Modulating NiO-Based Sensor Arrays," *Advanced Materials Technologies* 7 (2022): 2100762, https://doi.org/10.1002/admt.202100762.

28. H. Ma, T. Wang, B. Li, et al., "A Low-Cost and Efficient Electronic Nose System for Quantification of Multiple Indoor Air Contaminants Utilizing HC and PLSR," *Sensors and Actuators B: Chemical* 350 (2022): 130768, https://doi.org/10.1016/j.snb.2021.130768.

29. T. Wang, H. Zhang, Y. Wu, et al., "Classification and Concentration Prediction of VOCs with High Accuracy Based on an Electronic Nose Using an ELM-ELM Integrated Algorithm," *IEEE Sensors Journal* 22 (2022): 14458–14469, https://doi.org/10.1109/JSEN.2022.3176647.

30. M. Kang, I. Cho, J. Park, et al., "High Accuracy Real-Time Multi-Gas Identification by a Batch-Uniform Gas Sensor Array and Deep Learning Algorithm," *ACS Sensors* 7 (2022): 430–440, https://doi.org/10.1021/acssensors.1c01204.

31. H. Liu, G. Meng, Z. Deng, et al., "Discriminating BTX Molecules by the Nonselective Metal Oxide Sensor-Based Smart Sensing System," *ACS Sensors* 6 (2021): 4167–4175, https://doi.org/10.1021/acssensors.1c01704.

32. C. Fang, H. Y. Li, L. Li, et al., "Smart Electronic Nose Enabled by an All-Feature Olfactory Algorithm," *Advanced Intelligent Systems* 4 (2022): 2200074, https://doi.org/10.1002/aisy.202200074.

33. H. Bakiler and S. Güney, "Estimation of Concentration Values of Different Gases Based on Long Short-Term Memory by Using Electronic Nose," *Biomedical Signal Processing and Control* 69 (2021): 102908, https://doi.org/10.1016/j.bspc.2021.102908.

34. D. Karakaya, O. Ulucan, and M. Turkan, "Electronic Nose and Its Applications: A Survey," *International Journal of Automation and Computing* 17 (2020): 179–209, https://doi.org/10.1007/s11633-019-1212-9.

35. A. Zulkefli, B. Mukherjee, R. Sahara, et al., "Enhanced Selectivity in Volatile Organic Compound Gas Sensors Based on ReS_2-FETs under Light-Assisted and Gate-Bias Tunable Operation," *ACS Applied Materials & Interfaces* 13 (2021): 43030–43038, https://doi.org/10.1021/acsami.1c10054.

36. S. Hong, M. Wu, Y. Hong, et al., "FET-Type Gas Sensors: A Review," *Sensors and Actuators B: Chemical* 330 (2021): 129240, https://doi.org/10.1016/j.snb.2020.129240.

37. P. Zhang, Y. Xiao, J. Zhang, B. Liu, X. Ma, and Y. Wang, "Highly Sensitive Gas Sensing Platforms Based on Field Effect Transistor-A Review," *Analytica Chimica Acta* 1172 (2021): 338575, https://doi.org/10.1016/j.aca.2021.338575.

38. B. Sharma, A. Sharma, and J. S. Kim, "Recent Advances on H_2 Sensor Technologies Based on MOX and FET Devices: A Review," *Sensors and Actuators B: Chemical* 262 (2018): 758–770, https://doi.org/10.1016/j.snb.2018.01.212.

39. J. Zhang, L. Liu, Y. Yang, Q. Huang, D. Li, and D. Zeng, "A Review on Two-Dimensional Materials for Chemiresistive- and FET-Type Gas Sensors," *Physical Chemistry Chemical Physics* 23 (2021): 15420–15439, https://doi.org/10.1039/D1CP01890F.

40. S. Zhang, Z. Yuan, and F. Meng, "Electronic Nose under Dynamic Temperature Modulation for Highly Selective Identification of Industrial Toxic Chemicals," *IEEE Transactions on Instrumentation and Measurement* 74 (2025): 1–11, https://doi.org/10.1109/TIM.2025.3588944.

41. H. Liu, R. Wu, Q. Guo, Z. Hua, and Y. Wu, "Electronic Nose Based on Temperature Modulation of MOS Sensors for Recognition of Excessive Methanol in Liquors," *ACS Omega* 6 (2021): 30598–30606, https://doi.org/10.1021/acsomega.1c04350.

42. R. Ionescu, Y. Zilberman, and H. Haick, "Development of an Extremely Selective E-Nose Employing a Single Polycyclic Aromatic Hydrocarbon-Based chemFET," paper presented at *SENSORS, 2011 IEEE*, Limerick, Ireland, October 28-31, 2011, https://doi.org/10.1109/ICSENS.2011.6127311.

43. J. Janata, "Chemically Sensitive Field-Effect Transistors, Past, Present and Future," *ChemElectroChem* 9 (2022): e202200784, https://doi.org/10.1002/celc.202200784.

44. Y. Jiang, H. Tai, G. Xie, and J. Yu, "Fabrication and NO_2 Sensing Properties of ChemFET Sensors with Self-Assembly PAN/PSSA Sensitive Films Based on Nano-Au Surface," *Proceedings of SPIE* 6984 (2008): 69843Q, https://doi.org/10.1117/12.792244.

45. J. Sengupta and C. M. Hussain, "Graphene-Based Field-Effect Transistor Biosensors for the Rapid Detection and Analysis of Viruses: A Perspective in View of COVID-19," *Carbon Trends* 2 (2021): 100011, https://doi.org/10.1016/j.cartre.2020.100011.

46. E. K. Hong and W. J. Cho, "Semiconducting Single-Walled Carbon Nanotube Network-Based Double-Gate Thin-Film Transistors for High-Performance Aqueous Chemical Sensor Applications," *AIP Advances* 8 (2018): 115312, https://doi.org/10.1063/1.5059376.

47. A. Lale, A. Grappin, L. Mazenq, et al., "Development of All-Around SiO_2/Al_2O_3 Gate, Suspended Silicon Nanowire Chemical Field Effect

Transistors Si-Nw-ChemFET," *Proceedings* 1 (2017), 419, https://doi.org/10.3390/proceedings1040419.

48. S. V. Kalinin, J. Shin, S. Jesse, et al., "Electronic Transport Imaging in a Multiwire SnO_2 Chemical Field-Effect Transistor Device," *Journal of Applied Physics* 98 (2005): 044503, https://doi.org/10.1063/1.2001144.

49. N. Devabharathi, J. R. Pradhan, S. S. Priyadarsini, T. Brezesinski, and S. Dasgupta, "Inkjet-Printed Narrow-Channel Mesoporous Oxide-Based n-Type TFTs and all-Oxide CMOS Electronics," *Advanced Materials Interfaces* 9 (2022): 2200949, https://doi.org/10.1002/admi.202200949.

50. L. Zhu, G. He, J. Lv, E. Fortunato, and R. Martins, "Fully Solution-Induced High Performance Indium Oxide Thin Film Transistors with ZrOx High-K Gate Dielectrics," *RSC Advances* 8 (2018): 16788–16799, https://doi.org/10.1039/C8RA02108B.

51. C. H. Choi, S. Y. Han, Y. W. Su, et al., "Fabrication of High-Performance, Low-Temperature Solution Processed Amorphous Indium Oxide Thin-Film Transistors Using a Volatile Nitrate Precursor," *Journal of Materials Chemistry C* 3 (2015): 854–860, https://doi.org/10.1039/C4TC01568A.

52. H. Lee, X. Zhang, J. Kim, E. J. Kim, and J. Park, "Investigation of the Electrical Characteristics of Bilayer ZnO/In_2O_3 Thin-Film Transistors Fabricated by Solution Processing," *Materials* 11 (2018): 2103, https://doi.org/10.3390/ma11112103.

53. R. Yao, X. Fu, W. Li, et al., "Bias Stress Stability of Solution-Processed Nano Indium Oxide Thin Film Transistor," *Micromachines* 12 (2021): 111, https://doi.org/10.3390/mi12020111.

54. S. Shah, S. Hussain, S. T. U. Din, et al., "A Review on In_2O_3 Nanostructures for Gas Sensing Applications," *Journal of Environmental Chemical Engineering* 12 (2024): 112538, https://doi.org/10.1016/j.jece.2024.112538.

55. C. Li, D. Zhang, X. Liu, et al., "In_2O_3 Nanowires as Chemical Sensors," *Applied Physics Letters* 82 (2003): 1613–1615, https://doi.org/10.1063/1.1559438.

56. A. Chizhov, P. Kutukov, A. Astafiev, and M. Rumyantseva, "Photoactivated Processes on the Surface of Metal Oxides and Gas Sensitivity to Oxygen," *Sensors* 23 (2023): 1055, https://doi.org/10.3390/s23031055.

57. J. Fang, Z.-H. Ma, J.-J. Xue, X. Chen, R.-P. Xiao, and J.-M. Song, "Au Doped In_2O_3 Nanoparticles: Preparation, and Their Ethanol Detection with High Performance," *Materials Science in Semiconductor Processing* 146 (2022): 106701, https://doi.org/10.1016/j.mssp.2022.106701.

58. G. P. Gramlich, "Aerosol Jet and Ultra Precise Dispensing Printed Millimeter Wave Interconnects,"(PhD, Karlsruher Institute of Technology (KIT), 2025), https://doi.org/10.5445/IR/1000185006.

59. M. Nazarzadehmoafi, "Electronic Properties of Metal-In_2O_3 Interfaces," (Doctoral Dissertation, Technical University of Darmstadt (TU Darmstadt), 2017), https://doi.org/10.18452/17771.

60. D. Chen, Y. Jiang, Z. Sun, Y. Huang, J. Yu, and T. Chen, "ITO/Ag/ITO and ITO/Cu/ITO Transparent Rear Contacts for Semi-Transparent Perovskite Solar Cells," *Thin Solid Films* 752 (2022): 139252, https://doi.org/10.1016/j.tsf.2022.139252.

61. S. Kim, J. H. Jang, and J. S. Lee, "Thermally Stable and Highly Reflective ITO/Ag-Based Ohmic Contacts to p-GaN," *Journal of The Electrochemical Society* 154 (2007): H973, https://doi.org/10.1149/1.2778862.

62. Y. Zhou, *Semiconducting Metal Oxide Thin-Film Transistors* (IOP Publishing Ltd, 2021), https://doi.org/10.1088/978-0-7503-2556-1.

63. R. A. Fisher, "The Use of Multiple Measurements in Taxonomic Problems," *Annals of Eugenics* 7 (1936): 179–188, https://doi.org/10.1111/j.1469-1809.1936.tb02137.x.

64. V. Y. Musatov, V. V. Sysoev, M. Sommer, and I. Kiselev, "Assessment of Meat Freshness with Metal Oxide Sensor Microarray Electronic Nose: A Practical Approach," *Sensors and Actuators B: Chemical* 144 (2010): 99–103, https://doi.org/10.1016/j.snb.2009.10.040.

65. M. Adib, R. Eckstein, G. Hernandez-Sosa, M. Sommer, and U. Lemmer, "SnO_2 Nanowire-Based Aerosol Jet Printed Electronic Nose as Fire Detector," *IEEE Sensors Journal* 18 (2018): 494–500, https://doi.org/10.1109/JSEN.2017.2777178.

66. S. Zhao, B. Zhang, J. Yang, J. Zhou, and Y. Xu, "Linear Discriminant Analysis," *Nature Reviews Methods Primers* 4 (2024): 70, https://doi.org/10.1038/s43586-024-00346-y.

67. A. Tharwat, T. Gaber, A. Ibrahim, and A. E. Hassanien, "Linear Discriminant Analysis: A Detailed Tutorial," *AI Communications* 30 (2017): 169–190, https://doi.org/10.3233/AIC-170729.

68. S. Jeong, J. Kim, and J. Lee, "Rational Design of Semiconductor-Based Chemiresistors and Their Libraries for Next-Generation Artificial Olfaction," *Advanced Materials* 32 (2020): 2002075, https://doi.org/10.1002/adma.202002075.

69. A. M. Teli, S. M. Mane, S. A. Beknalkar, R. K. Mishra, W. Jeon, and J. C. Shin, "Recent Advances in Metal–Organic Frameworks for Gas Sensors: Design Strategies and Sensing Applications," *Sensors* 26 (2026): 956, https://doi.org/10.3390/s26030956.

70. T. Doll, ed., *Advanced Gas Sensing—The Electroadsorptive Effect and Related Techniques* (Springer US, 2003), https://doi.org/10.1007/978-1-4419-8612-2.

71. T. Doll, J. J. Velasco-Velez, D. Rosenthal, J. Avila, and V. Fuenzalida, "Direct Observation of the Electroadsorptive Effect on Ultrathin Films for Microsensor and Catalytic-Surface Control," *Chemphyschem* 14 (2013): 2505–2510, https://doi.org/10.1002/cphc.201201013.

72. C. Bur, "Selectivity Enhancement of Gas Sensitive Field Effect Transistors by Dynamic Operation," (PhD, Linkopings Universitet, 2015).

73. S. A. Singaraju, "Development of Fully Printed Oxide Electronics for Flexible Substrates," (PhD, Karlsruher Institute of Technology (KIT), 2021), https://doi.org/10.5445/IR/1000131808.

74. S. A. Singaraju, G. C. Marques, P. Gruber, et al., "Fully Printed Inverters Using Metal-Oxide Semiconductor and Graphene Passives on Flexible Substrates," *physica status solidi (RRL)—Rapid Research Letters* 14 (2020): 2000252, https://doi.org/10.1002/pssr.202000252.

75. S. A. Singaraju, T. T. Baby, F. Neuper, et al., "Development of Fully Printed Electrolyte-Gated Oxide Transistors Using Graphene Passive Structures," *ACS Applied Electronic Materials* 1 (2019): 1538–1544, https://doi.org/10.1021/acsaelm.9b00313.

76. R. Henrion, G. Henrion, and M. Datenanalyse, *Multivariate Datenanalyse–Methodik und Anwendung in der Chemie und verwandten Gebieten* (Springer, 1995), https://doi.org/10.1007/978-3-642-57792-5.

Supporting Information

Additional supporting information can be found online in the Supporting Information section.

Supporting File: adsr70194-sup-0001-SuppMat.docx.